

SYNTHESIS, CHARACTERIZATION AND POTENTIAL APPLICATION OF $Zn_3(Ta_{1-x}Nb_x)_2O_8$ OXIDES

M. BÎRDEANU^{a,b*}, I. SEBARCHIEVICI^b, A.V. BÎRDEANU^c, B. ȚĂRANU^b,
F. PETER^a, E. FAGADAR-COSMA^d

^a*Politehnica University of Timisoara, Vasile Parvan Ave.6, 300223-Timisoara, Romania*

^b*National Institute for Research and Development in Electrochemistry and Condensed Matter, 1 Plautius Andronescu Street, 300224 Timisoara, Romania*

^c*National R&D Institute for Welding and Material Testing - ISIM Timișoara, 20 M. Viteazu Ave., 300222, Timisoara, Romania*

^d*Institute of Chemistry Timisoara of Romanian Academy, 24 M. Viteazu Ave, 300223-Timisoara, Romania*

Nanomaterials based on pseudo-binary oxides $Zn_3(Ta_{1-x}Nb_x)_2O_8$ (where $x = 0; 0.05; 0.1; 0.5$ and 1) were obtained by solid-state method varying the molar ratios of tantalum (V) oxide, niobium (V) oxide and zinc oxide. Three of these nanomaterials are based on novel structures, namely: $Zn_3(Ta_{0.5}Nb_{0.5})_2O_8$, $Zn_3(Ta_{0.9}Nb_{0.1})_2O_8$ and $Zn_3(Ta_{0.95}Nb_{0.05})_2O_8$. The structures of the above mentioned nanomaterials were thoroughly characterized by X-ray diffraction, FT-IR, UV-VIS and PL spectroscopy, SEM and AFM microscopy techniques. A potential application of these nanomaterials as corrosion inhibitors is presented. The property of corrosion inhibition was demonstrated by electrochemical methods, such as: open circuit potential measurement and potentiodynamic polarization with Tafel representation. The studies were performed on all obtained pseudo-binary oxides $Zn_3(Ta_{1-x}Nb_x)_2O_8$ (where $x = 0; 0.05; 0.1; 0.5$ and 1) after their deposition onto carbon steel surfaces (OL) in 0.1 mole/L Na_2SO_4 media. The experiments revealed that the corrosion protection is fairly good for all tested nanomaterials and that the electrode modified with $Zn_3Ta_2O_8$ presented a top inhibition efficiency of 56.49%.

(Received March 14, 2015; Accepted May 23, 2015)

Keywords: solid-state method, pseudo-binary oxides, nanomaterials, Tafel curves, XRD

1. Introduction

$Zn_3Ta_2O_8$ and $Zn_3Nb_2O_8$ have been studied as luminescent and dielectric host materials [1] and their synthesis are currently based on several modern chemistry preparation routes, e.g. co-precipitation [2], hydrothermal reaction [3, 4], besides the more conventional solid-state reaction of mixed oxides [5–8].

In the last years, binary compounds having $Zn_3(Ta_{1-x}Nb_x)_2O_8$ as their general formula, were identified as proper candidates for low voltage cathodoluminescent materials. The envisaged applications for wide scale usage are related to flat panel display technologies (for field emission displays -FEDs and vacuum fluorescent displays -VFDs) [8–11].

Other spinel materials were investigated with respect to their applicability as low voltage cathodoluminescent (CL) materials, especially sulfide based phosphors [12, 13]. However, the volatility of sulfur contained in these materials limits its usage in FEDs or VFDs and produces harmful effects on these devices:

*Corresponding author: mihaelabirdeanu@gmail.com

- a sulfur deficient in luminescence layer degrades the phosphor efficiency being related to possible electron stimulated reactions that generates by-products [14];
- the poisoning of the electron emitters [9].

Nowadays, an increased demand to protect the environment by reducing and monitoring all causes that could damage and pollute the environment and society can be noticed. One of those major causes is corrosion. Corrosion can damage almost all types of materials that are used in all kinds of industries, e.g. materials used to build cars, water pipeline systems, buildings, even petroleum constructions (pipelines, refineries) [15, 16].

The corrosion related risks require the introduction of inhibitors of corrosion for technological equipments. The application of corrosion inhibitors can provide several-fold decrease in the oxygen corrosion of steel in aggressive aqueous media, thus increasing the life time of expensive oil and chemical equipments [17-21].

Steel is a widely used engineering material and can be found in a range of industries: from mechanical manufacturing, constructions, defense and transportation, to medical appliances [22]. The corrosion process of steel is usually spontaneous as a result of chemical or electrochemical reactions with its environment and it can compromise the integrity of steel based components, which in turn can have a smaller or greater impact on the environment, as long as people don't take (proper) measures to prevent or control it.

Although the most widely used material for corrosion protection of steel remains Zn [22], its resistance is limited. This is the reason why, during the last decade, an important amount of researches focused on alloying Zn with more noble metals or inducing surface inhibitors [23]. Zn alloys provide better corrosion resistance of ferrous based materials [24-27]. Also in the last decade, a trend can be observed in using niobium and tantalum in chemical processing applications, due to the fact that they present good corrosion resistance in a variety of corrosive environments, from organic acids to liquid metals.

Following this trend, the present paper describes the results of an experimental study focused on the synthesis by the solid-state method of nanocrystalline compounds $Zn_3(Ta_{1-x}Nb_x)_2O_8$ (where $x=1; 0.5; 0.1; 0.05$ and 0), their physico-chemical characterization emphasizing their corrosion protection properties. The corrosion protection provided by these materials was assessed through electrochemical methods, such as: open circuit potential measurement and potentiodynamic polarization method with Tafel representation. The studies were performed regarding all synthesized pseudo-binary oxides after their deposition onto carbon steel surfaces (OL) from 0.1 mole/L Na_2SO_4 media.

2. Experimental procedure

Method for obtaining of $Zn_3(Ta_{1-x}Nb_x)_2O_8$ (where $x = 0; 0.05; 0.1; 0.5$ and 1)

The $Zn_3(Ta_{1-x}Nb_x)_2O_8$ (where $x = 0; 0.05; 0.1; 0.5$ and 1) nanomaterials were obtained by solid-state method varying the molar ratios, in accordance with Table 1. The starting materials used during the synthesis were: tantalum (V) oxide - Ta_2O_5 (99.99%, Merck), niobium (V) oxide - Nb_2O_5 (99.99%, Merck) and zinc oxide - ZnO (99.99%, Merck). Each mixture of oxides (Table 1) was afterwards heated at 1200 °C for 3 h soaking time. The heating and cooling rate of the heated furnace was set at 5 °C/min.

Table 1. The $Zn_3(Ta_{1-x}Nb_x)_2O_8$ nanomaterials obtained by solid-state method

The Obtained naomaterials	x	Molar Ratios
$Zn_3Ta_2O_8$	0	$ZnO/Ta_2O_5=3/1$
$Zn_3Nb_2O_8$	1	$ZnO/Nb_2O_5=3/1$
$Zn_3(Ta_{0.95}Nb_{0.05})_2O_8$	0.05	$ZnO/Ta_2O_5/Nb_2O_5=3/0.95/0.05$
$Zn_3(Ta_{0.9}Nb_{0.1})_2O_8$	0.1	$ZnO/Ta_2O_5/Nb_2O_5=3/0.9/0.1$
$Zn_3(Ta_{0.5}Nb_{0.5})_2O_8$	0.5	$ZnO/Ta_2O_5/Nb_2O_5=3/0.5/0.5$

Method for electrode preparations

Before each experiment, the electrode surface was mechanically polished to a mirror-like surface using emery paper of different grades, rinsed with double distilled water, degreased with ethanol. Powder samples of $Zn_3(Ta_{1-x}Nb_x)_2O_8$ (where $x = 0; 0.05; 0.1; 0.5$ and 1) were dissolved under aggressive conditions in a mixture of HF and H_2SO_4 in vol/vol ratio of 3/1 for 2 hours, at $200^\circ C$ and subsequently diluted with a controlled volume of double distilled water. The OL electrodes were further immersed in the pseudo-binary oxide solutions. The immersion time for each experiment was 5 minutes at the room temperature. After this step, passive layers containing the nanomaterials were formed on the surface of OL electrodes. After immersion, the modified electrode was rinsed with water and transferred as rapidly as possible into the electrochemical cell for corrosion testing. Control samples were not modified with solutions containing $Zn_3(Ta_{1-x}Nb_x)_2O_8$ (where $x = 0; 0.05; 0.1; 0.5$ and 1) nanomaterials.

The corrosion behaviour was studied using a Voltalab potentiostat Model PGZ 402 with VoltaMaster 4 software v.7.09. This software analyzed the potentiodynamic polarization curves, performed the Tafel fitting and calculated the values of the corrosion potential (E_{corr}), corrosion current density (i_{corr}) and corrosion rate (v_{corr}). A single compartment three-electrode cell was employed along with a platinum wire as the counter electrode and the saturated calomel electrode (SCE) as reference electrode. All potentials reported in this article are referenced to the Standard Hydrogen Electrode (SHE). Bare and coated carbon steel (OL) disks, having the chemical composition presented in Table 2, were employed as working electrodes. The electrodes were mounted into a Teflon body used for ensuring a good electrical contact and an active constant surface of 0.28 cm^2 .

Table 2. Chemical composition of carbon steel (OL).

Element	C	Si	Mn	P	S	Fe
Percentages (%)	0.12-0.18	0.10-0.35	0.70-1.10	0.03	0.07-0.13	98.21-98.98

The potentiodynamic polarization measurements were performed by sweeping the potential between -1.3 and 0.2 V , in $0.1\text{ mole/L Na}_2\text{SO}_4$ electrolyte solution, at a scan rate (v) of 1 mV/s .

Apparatus

The phase identification of the synthesized powders was performed using X-ray diffraction (XRD) on an X'pert Pro MPD X-ray diffractometer, with monochromatic $Cu\ K\alpha$ ($\lambda = 1.5418\text{ \AA}$) incident radiation. FT-IR measurements were performed on a JASCO 430 FT-IR spectrometer, in the $4000-400\text{ cm}^{-1}$ spectral range, using KBr pellets. The morphology and the size of the sample particles were investigated by field emission-scanning electron microscopy – SEM / EDAX (Model INSPECT S), and atomic force microscopy – AFM (Model Nanosurf® EasyScan 2 Advanced Research). The band gap of the $Zn_3(Ta_{1-x}Nb_x)_2O_8$ ($x = 0; 0.05; 0.1; 0.5$ and 1) nanocrystals was calculated by recording the diffuse reflectance spectrum at room temperature, using a UV-VIS-NIR spectrometer Lambda 950. The PL spectra were recorded with a Perkin Elmer LS55 luminescence spectrometer, by using a special holder for powder solid samples. The luminescence spectra were recorded at 100 nm/min with slit widths (i.e. 15 nm for excitation and 2.5 nm for emission). The emission spectra were obtained using an excitation wavelength of 250 nm and a 430 nm cut-off filter was applied in order to eliminate the harmonic(s) or the scattering peaks.

The corrosion behaviour was studied using a Voltalab potentiostat Model PGZ 402 with VoltaMaster 4 software v.7.09.

3. Results and Discussions

3.1 Structural characterization

The X-ray diffraction patterns obtained at room temperature for the synthesized nanomaterials: $Zn_3Ta_2O_8$, $Zn_3(Ta_{0.95}Nb_{0.05})_2O_8$, $Zn_3(Ta_{0.9}Nb_{0.1})_2O_8$, $Zn_3(Ta_{0.5}Nb_{0.5})_2O_8$ and $Zn_3Nb_2O_8$, are presented in Figure 1, where the crystallographic planes (h k l) are indicated. The recorded spectra were compared to the spectra of pure nanomaterials $Zn_3Ta_2O_8$ and $Zn_3Nb_2O_8$ found in the indexed database. It can be observed that besides the main peak associated with the $Zn_3Ta_2O_8$ and $Zn_3Nb_2O_8$, some associated peaks are also present (indexed with JCPDS, card No. 00-020-1237 and 01-050-1725) [28].

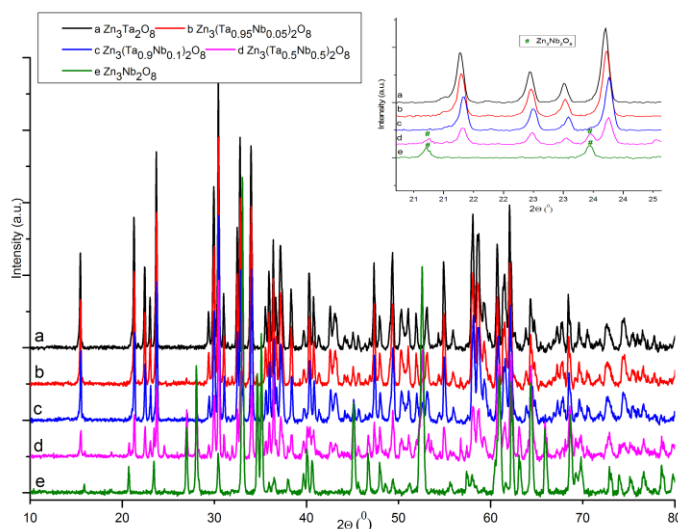


Fig. 1. XRD patterns of (a) $Zn_3Ta_2O_8$, (b) $Zn_3(Ta_{0.95}Nb_{0.05})_2O_8$, (c) $Zn_3(Ta_{0.9}Nb_{0.1})_2O_8$, (d) $Zn_3(Ta_{0.5}Nb_{0.5})_2O_8$ and (e) $Zn_3Nb_2O_8$. A magnified zone of XRD patterns was inserted.

The intensity of the peaks [Figure 1, (a) and (e)] relative to the background signal, demonstrates the high purity of the samples.

In figure 1(a) it can be seen that the most intense peak appears at $2\theta = 30.487^\circ$ and corresponds to the crystallographic plane (-113). $Zn_3Ta_2O_8$ nanomaterial belongs to the symmetry group C2/c. The lattice parameters were calculated using the FullProf Suite program [29]: $a = 9.53 \text{ \AA}$, $b = 8.39 \text{ \AA}$ and $c = 8.90 \text{ \AA}$, the angles $\alpha = \gamma = 90^\circ$ and $\beta = 116.39^\circ$, and the volume of the unit cell $\text{vol.} = 636.991 \text{ (V/10}^6\text{/pm}^3\text{)}$.

In figure 1(e) the most intense peak appears at $2\theta = 33.038^\circ$ and is attributed to the crystallographic plane (-511). The $Zn_3Nb_2O_8$ nanomaterial belongs to the symmetry group C2/c. The calculated lattice parameters were: $a = 19.093 \text{ \AA}$, $b = 5.927 \text{ \AA}$ and $c = 5.220 \text{ \AA}$, angles $\alpha = \beta = \gamma = 90^\circ$, and the volume of the unit cell $\text{vol.} = 570.72 \text{ (V/10}^6\text{/pm}^3\text{)}$.

The peak sites have different intensities (figures 1 b, c and d), in accordance with the concentrations used for niobium and tantalum, respectively. Increasing the concentration of Nb the appearance of the $Zn_3Nb_2O_8$ specific peaks can be observed (a plot representing the magnified zone of XRD patterns was inserted in Figure 1).

The mean crystallite size (d) of the powder samples was calculated using Scherrer's formula [30]. The average crystallite sizes determined from XRD line broadening for each of the samples were: 10 nm for $Zn_3Ta_2O_8$, 12 nm for $Zn_3(Ta_{0.95}Nb_{0.05})_2O_8$, 14 nm for $Zn_3(Ta_{0.9}Nb_{0.1})_2O_8$, 19 nm for $Zn_3(Ta_{0.5}Nb_{0.5})_2O_8$ and 25 nm for $Zn_3Nb_2O_8$. The value is increasing with the increase of the Nb content of the nanomaterial.

Besides the X-ray diffraction analysis, FT-IR spectroscopy measurements were carried out in order to determine the existence of non-crystalline phases, which could be present in the mixture along with the crystalline phases.

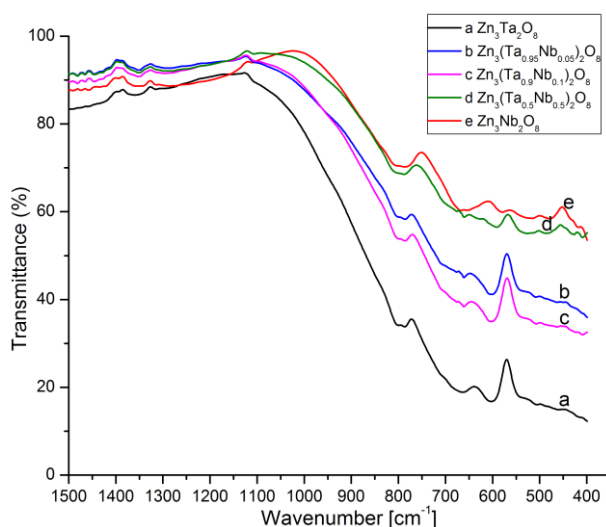


Fig.2. FT/IR spectra of the synthesized nanomaterials (a) $Zn_3Ta_2O_8$, (b) $Zn_3(Ta_{0.95}Nb_{0.05})_2O_8$, (c) $Zn_3(Ta_{0.9}Nb_{0.1})_2O_8$, (d) $Zn_3(Ta_{0.5}Nb_{0.5})_2O_8$ and (e) $Zn_3Nb_2O_8$

Figure 2 presents the FT/IR spectra of the synthesized nanomaterials: $Zn_3Ta_2O_8$, $Zn_3Nb_2O_8$, $Zn_3(Ta_{0.95}Nb_{0.05})_2O_8$, $Zn_3(Ta_{0.9}Nb_{0.1})_2O_8$ and $Zn_3(Ta_{0.5}Nb_{0.5})_2O_8$. The spectra were recorded by transmittance in the range of $1,500-390\text{cm}^{-1}$.

The FT-IR spectra of the newly obtained compounds ($Zn_3(Ta_{1-x}Nb_x)_2O_8$ ($x = 0; 0.05; 0.1; 0.5$ and 1)) displayed some distinctive bands, located at 572cm^{-1} for $Zn_3Ta_2O_8$, 449cm^{-1} for $Zn_3Nb_2O_8$, 573cm^{-1} for $Zn_3(Ta_{0.95}Nb_{0.05})_2O_8$, 572cm^{-1} for $Zn_3(Ta_{0.9}Nb_{0.1})_2O_8$ and two bands located at 569 and 454cm^{-1} for $Zn_3(Ta_{0.5}Nb_{0.5})_2O_8$, respectively.

In the spectra recorded for $Zn_3Ta_2O_8$ it can be noticed a novel band located at 572cm^{-1} (not present in the spectra of simple oxides ZnO and Ta_2O_5) that might be attributed to the Zn-O-Ta bond [4, 31]. Also, in the spectra of the $Zn_3Nb_2O_8$ nanomaterial, a new band located at 449cm^{-1} distinctively different from Nb-O and Zn-O, can be assigned to Zn-O-Nb bonds. By decreasing the amount of Nb from the nanomaterial composition, the corresponding Zn-O-Nb bond is shifted towards higher wavenumbers.

3.2 Morphological characterization

The morphological aspect of the resulting powders, after deposition on OL surfaces, was examined by SEM and the resulting micrographs, recorded at a magnification of 3,000X, are shown in Fig. 3.

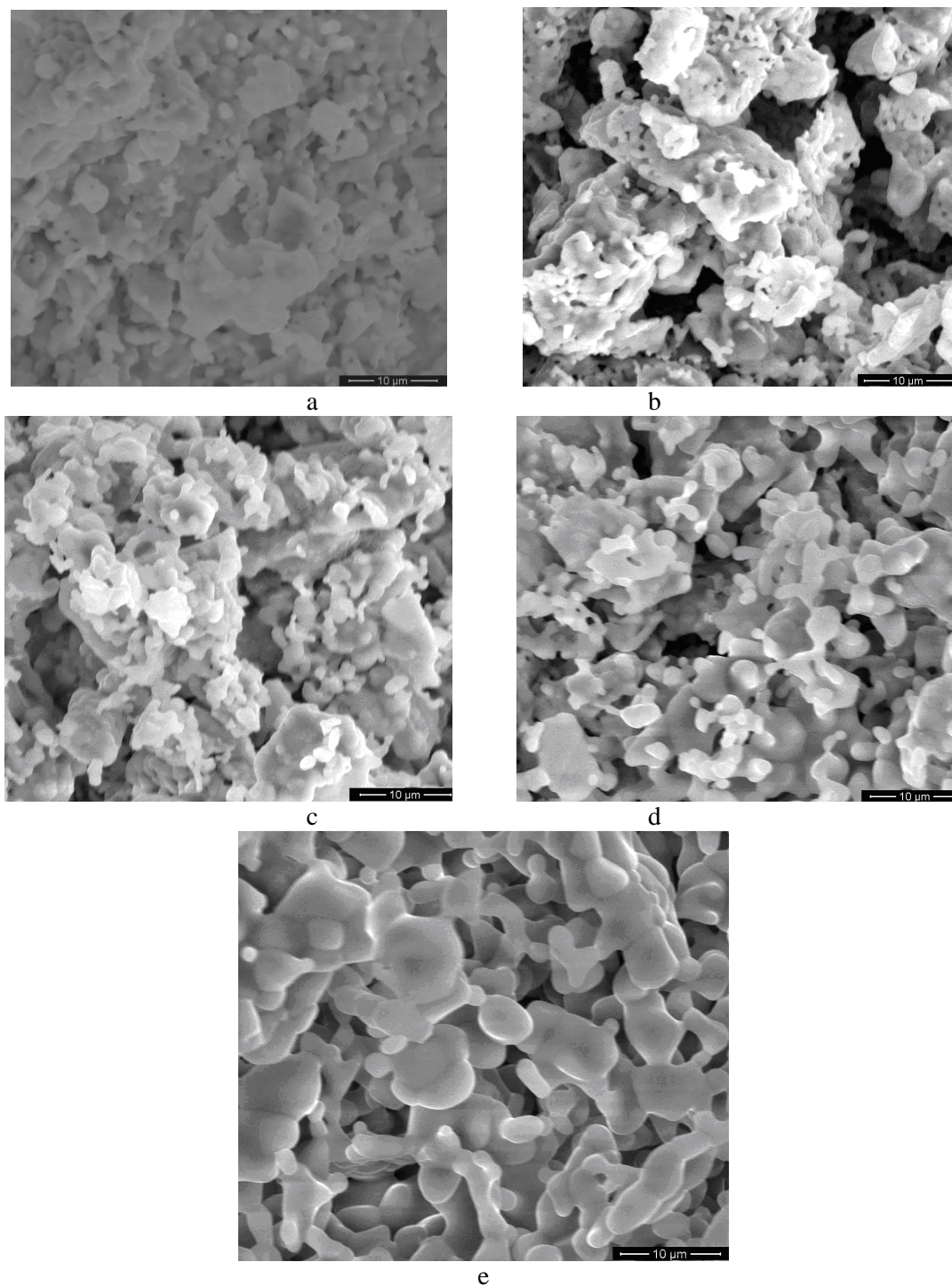


Fig. 3. SEM micrographs of: (a) $Zn_3Ta_2O_8$, (b) $Zn_3(Ta_{0.95}Nb_{0.05})_2O_8$, (c) $Zn_3(Ta_{0.9}Nb_{0.1})_2O_8$, (d) $Zn_3(Ta_{0.5}Nb_{0.5})_2O_8$ and (e) $Zn_3Nb_2O_8$, deposited on OL surfaces

Fig. 3 (a) shows non-uniform and randomly dispersed spherical or ovoid and heavily compacted structures comprised of $Zn_3Ta_2O_8$ particles and figure 4 (e) outlines the tendency of $Zn_3Nb_2O_8$ particles to form more uniform sized rods or blades. The various observed morphologies are depending on the nature and chemical composition of the nanomaterials: crystals multilayer organized in case of $Zn_3Nb_2O_8$, with an uniform covering aspect or various size distributed crystals, with porous or even sponge like shape in case of (d) $Zn_3(Ta_{0.5}Nb_{0.5})_2O_8$, (c) $Zn_3(Ta_{0.9}Nb_{0.1})_2O_8$, (b) $Zn_3(Ta_{0.95}Nb_{0.05})_2O_8$, with both mesopores and macropores (and a touch of amorphous aspect in case of Figure 3, a b and c, that corresponds to a large amount of Ta).

Figure 4 (a-e) shows the EDAX spectra for $Zn_3Ta_2O_8$, $Zn_3(Ta_{0.95}Nb_{0.05})_2O_8$, $Zn_3(Ta_{0.9}Nb_{0.1})_2O_8$, $Zn_3(Ta_{0.5}Nb_{0.5})_2O_8$ and $Zn_3Nb_2O_8$, obtained by solid-state synthesis and deposited on OL samples.

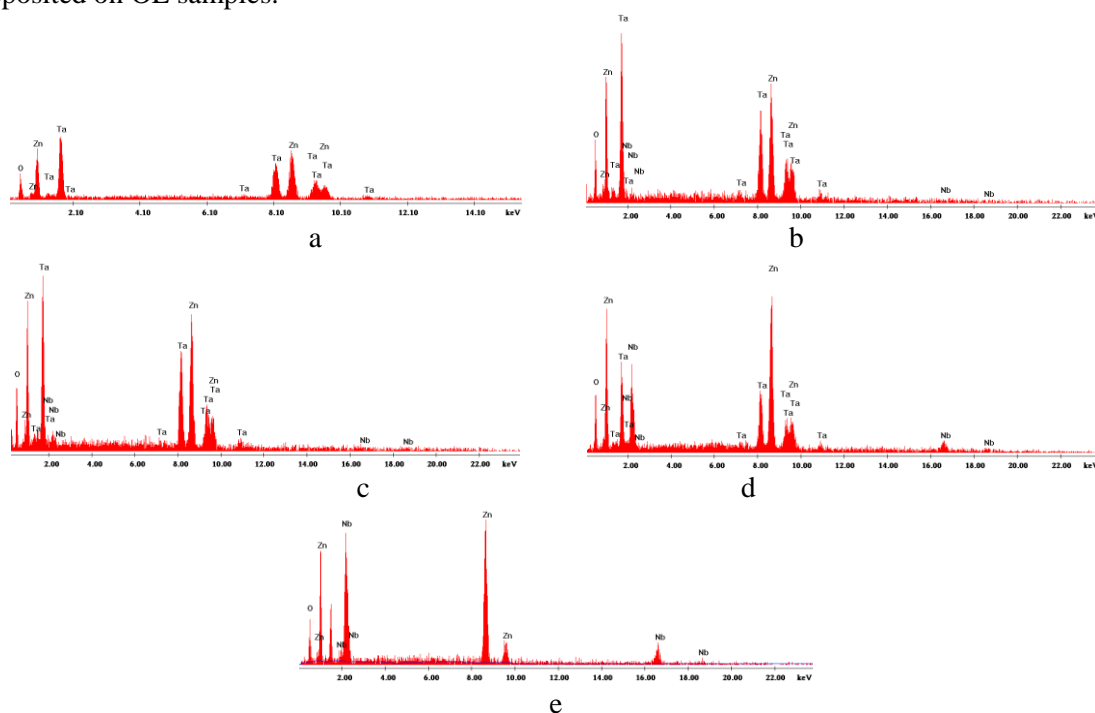


Fig. 4. EDAX spectra recorded for: (a) $Zn_3Ta_2O_8$, (b) $Zn_3(Ta_{0.95}Nb_{0.05})_2O_8$, (c) $Zn_3(Ta_{0.9}Nb_{0.1})_2O_8$, (d) $Zn_3(Ta_{0.5}Nb_{0.5})_2O_8$ and (e) $Zn_3Nb_2O_8$

The oxygen (O) is present as solely peak in all obtained samples at 0.515 eV, specifically to the energetic level K. The zinc (in all samples) presents two principal peaks corresponding to the energetic levels L and K. For the energetic level L, Zn has 1.014 eV and for the energetic level K, it has 8.628 eV. Due to its stable isotopes, each main peak of Zn has a secondary peak as pair. The tantalum EDAX diagram (figure 4 a-d) presents two main peaks corresponding to the energetic levels L (2 eV) and K (8.10 eV) accompanied by secondary peak pairings. In the EDAX spectrum (figure 4b-e) of the $Zn_3Nb_2O_8$ nanomaterial, the niobium presents two main peaks corresponding to the energetic levels L (2.10 eV) and K (17 eV), paired by secondary peaks.

The dimensions of the particles present on the scanned surfaces were measured using the AFM software. Figure 5 shows the distribution of particle dimensions on the surface of OL samples modified with $Zn_3Ta_2O_8$, $Zn_3(Ta_{0.95}Nb_{0.05})_2O_8$, $Zn_3(Ta_{0.9}Nb_{0.1})_2O_8$, $Zn_3(Ta_{0.5}Nb_{0.5})_2O_8$ and $Zn_3Nb_2O_8$.

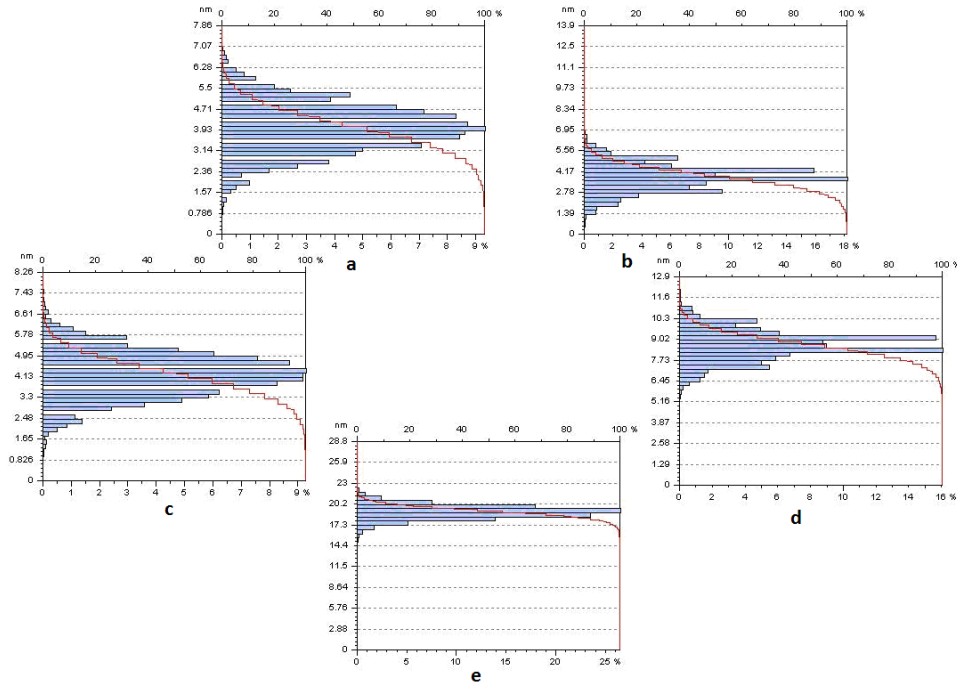


Fig. 5. The particle size distribution for (a) $Zn_3Ta_2O_8$, (b) $Zn_3(Ta_{0.95}Nb_{0.05})_2O_8$, (c) $Zn_3(Ta_{0.9}Nb_{0.1})_2O_8$, (d) $Zn_3(Ta_{0.5}Nb_{0.5})_2O_8$ and (e) $Zn_3Nb_2O_8$, on the surface of OL samples

It was found that: the dimensions of $Zn_3Ta_2O_8$ particles were between 2 and 7 nm; those of $Zn_3(Ta_{0.95}Nb_{0.05})_2O_8$ varied between 3 and 7 nm; for $Zn_3(Ta_{0.9}Nb_{0.1})_2O_8$ the dimensions ranged between 3 and 7.5 nm; in case of $Zn_3(Ta_{0.5}Nb_{0.5})_2O_8$ particles had sizes in the range 6.5 ÷ 11 nm and for $Zn_3Nb_2O_8$ the particle dimensions were between 17 and 23 nm (figure 5, a-e). In conclusion, the increase in Nb content causes a significant increase regarding the particle size. Besides particle size analysis, AFM measurements were also used to determine the surface roughness. The surface roughness was calculated using the equations [32], for the average roughness (Eq.2):

$$S_a = \frac{1}{MN} \sum_{k=0}^{M-1} \sum_{l=0}^{N-1} |z(x_k, y_l)| \quad (\text{Eq.2})$$

and the mean square root roughness (Eq.3), respectively:

$$S_q = \sqrt{\frac{1}{MN} \sum_{k=0}^{M-1} \sum_{l=0}^{N-1} (z(x_k, y_l))^2} \quad (\text{Eq.3})$$

where: N and M represent the number of crystallites on the x and y axis; z is the medium height of the crystallites; x_k and y_l are the maximum and minimum of the crystallites reported to the average value. The measured values (1,243 pm^2 area) of S_a and S_q for the nanomaterials were: $S_a = 0.31$ nm and $S_q = 0.4$ nm for $Zn_3Ta_2O_8$; $S_a = 0.33$ nm and $S_q = 0.45$ nm for $Zn_3(Ta_{0.95}Nb_{0.05})_2O_8$; $S_a = 0.37$ nm and $S_q = 0.52$ nm for $Zn_3(Ta_{0.9}Nb_{0.1})_2O_8$; $S_a = 0.4$ nm and $S_q = 0.60$ nm for $Zn_3(Ta_{0.5}Nb_{0.5})_2O_8$ and $S_a = 0.44$ nm and $S_q = 0.79$ nm for $Zn_3Nb_2O_8$, respectively. As already remarked, there is a direct relation between the higher content of Nb and the increased value of rugosity.

3.3 Optical properties

The diffuse reflectance spectra of $Zn_3Ta_2O_8$, $Zn_3(Ta_{0.95}Nb_{0.05})_2O_8$, $Zn_3(Ta_{0.9}Nb_{0.1})_2O_8$, $Zn_3(Ta_{0.5}Nb_{0.5})_2O_8$ and $Zn_3Nb_2O_8$ nanomaterials, in the 230-600 nm UV-VIS region, are shown in Figure 6.

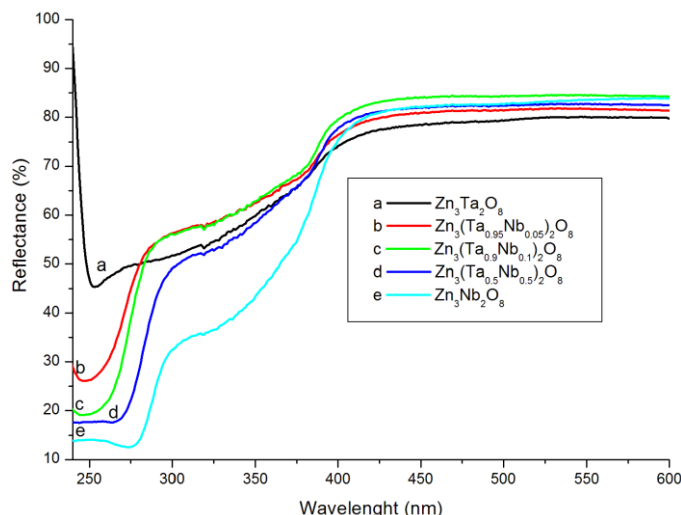


Fig. 6. Diffuse reflectance spectra of: (a) $Zn_3Ta_2O_8$, (b) $Zn_3(Ta_{0.95}Nb_{0.05})_2O_8$, (c) $Zn_3(Ta_{0.9}Nb_{0.1})_2O_8$, (d) $Zn_3(Ta_{0.5}Nb_{0.5})_2O_8$ and (e) $Zn_3Nb_2O_8$ nanomaterials

The absorbance was calculated from the reflectance using Kubelka-Munk equation [33, 34]. The optical absorption spectra (Figure 7) of the $Zn_3Ta_2O_8$, $Zn_3(Ta_{0.95}Nb_{0.05})_2O_8$, $Zn_3(Ta_{0.9}Nb_{0.1})_2O_8$, $Zn_3(Ta_{0.5}Nb_{0.5})_2O_8$ and $Zn_3Nb_2O_8$ nanomaterials, were detected in the 240-480 nm range, at ambient conditions. From each of the absorption spectra, the $\{(k/s)hv\}^2$ versus hv was plotted (Figure 7), where k denotes the absorption coefficient, "s" is the scattering coefficient and hv is the photon energy.

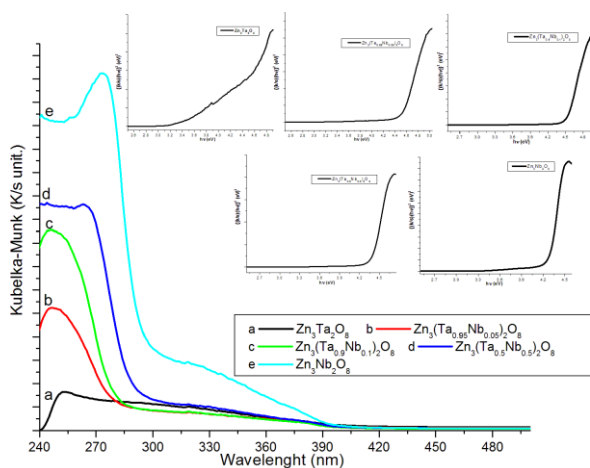


Fig. 7. The absorption spectra of: (a) $Zn_3Ta_2O_8$, (b) $Zn_3(Ta_{0.95}Nb_{0.05})_2O_8$, (c) $Zn_3(Ta_{0.9}Nb_{0.1})_2O_8$, (d) $Zn_3(Ta_{0.5}Nb_{0.5})_2O_8$ and (e) $Zn_3Nb_2O_8$. Plot of $\{(k/s)hv\}^2$ vs. hv (energy) of: $Zn_3Ta_2O_8$, $Zn_3(Ta_{0.95}Nb_{0.05})_2O_8$, $Zn_3(Ta_{0.9}Nb_{0.1})_2O_8$, $Zn_3(Ta_{0.5}Nb_{0.5})_2O_8$ and $Zn_3Nb_2O_8$

The band gap was calculated from Figure 7 and its value was 4.50 eV for $Zn_3Ta_2O_8$, 4.48 eV for $Zn_3(Ta_{0.95}Nb_{0.05})_2O_8$, 4.47 eV for $Zn_3(Ta_{0.9}Nb_{0.1})_2O_8$, 4.40 eV for $Zn_3(Ta_{0.5}Nb_{0.5})_2O_8$ and 4.28 eV for $Zn_3Nb_2O_8$. The values of the band gap are decreasing in direct relationship with the increasing in Nb content.

The PL spectra recorded in the 400-700 nm range for $Zn_3Ta_2O_8$, $Zn_3Nb_2O_8$, $Zn_3(Ta_{0.95}Nb_{0.05})_2O_8$, $Zn_3(Ta_{0.9}Nb_{0.1})_2O_8$ and $Zn_3(Ta_{0.5}Nb_{0.5})_2O_8$ are presented in figure 8.

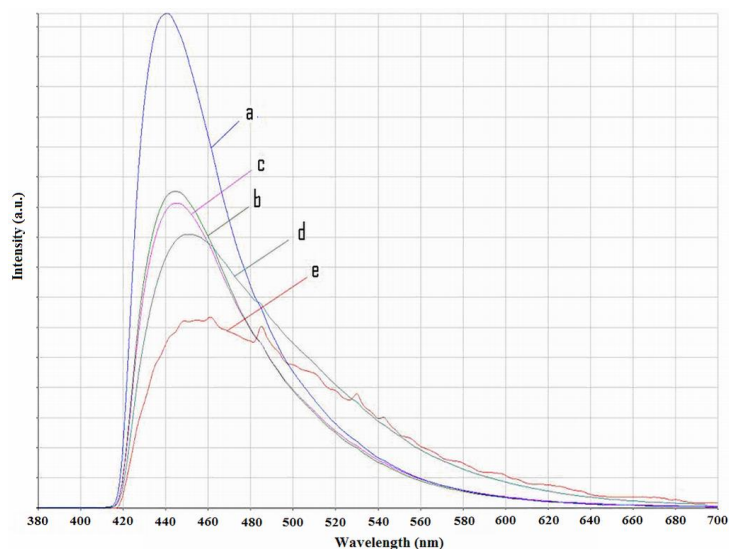


Fig. 8. PL spectra of the synthesized nanomaterials: (a) $Zn_3Ta_2O_8$, (b) $Zn_3(Ta_{0.95}Nb_{0.05})_2O_8$, (c) $Zn_3(Ta_{0.9}Nb_{0.1})_2O_8$, (d) $Zn_3(Ta_{0.5}Nb_{0.5})_2O_8$ and (e) $Zn_3Nb_2O_8$

The PL spectra show only single peaks at: 440 nm for $Zn_3Ta_2O_8$, 460 nm for $Zn_3Nb_2O_8$, 447 nm for $Zn_3(Ta_{0.95}Nb_{0.05})_2O_8$, 447 nm for $Zn_3(Ta_{0.9}Nb_{0.1})_2O_8$ and 450 nm for $Zn_3(Ta_{0.5}Nb_{0.5})_2O_8$, corresponding to the blue color. The results suggest that the intrinsic blue luminescence of the investigated nanomaterials is due to a metal-to-oxygen transition. [35]. By increasing the Nb content, a more pronounced red shift is occurring, from 447 nm up to 460 nm.

3.4 Corrosion inhibition study by Open circuit potential (OCP)

This analyze provides preliminary information on the nature of the processes occurring at the metal protective film/electrolyte interfaces. The open circuit potential or the free potential is a qualitative indicator of the state of corrosion of a metal substrate in an electrolytic medium and it also helps to determine the immersion time required for reaching the steady state.

The OCP versus time measurements (Figure 9) were performed in 0.1 mole/L Na_2SO_4 electrolyte solution for 30 minutes.

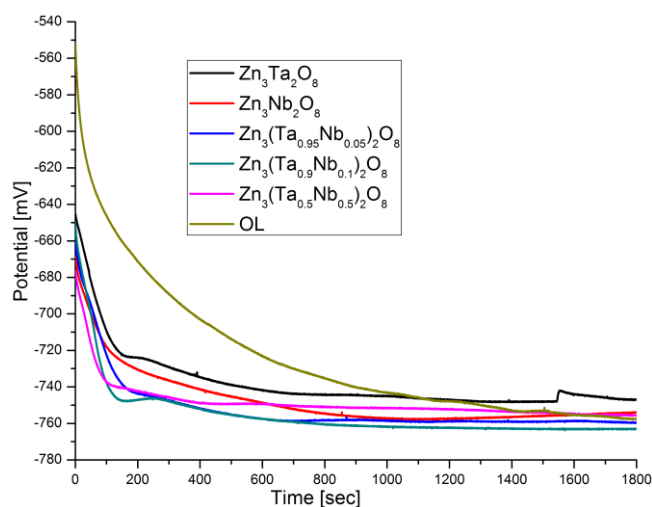


Fig. 9. Evolution of open circuit potential with time for investigated electrodes, in 0.1 mole/L Na_2SO_4 electrolyte solution

An initial analysis of these curves shows that in all cases including steel, a 30 minute exposure time leads to a shift in the free potential toward more negative values. Comparing the OCP profiles obtained for the coated electrodes with the profile obtained for the uncoated electrode, it can be observed that the former reached the steady state potential significantly faster (10 minutes) than the latter. At the end of the exposure time, the obtained OCP value of the $Zn_3Ta_2O_8$ electrode was nobler than the OCP values of the other electrodes.

3.5 Tafel polarization plots

The potentiodynamic cathodic and anodic polarization curves measured in 0.1 mole/L Na_2SO_4 solution, after 30 minutes stabilization of OCP, are presented in Figure 10 and the electrochemical parameters obtained from the Tafel extrapolation are summarized in Table 3. The degree of inhibition efficiency $IE(\%)$ has been calculated on the basis of equation 1 [36]:

$$IE\% = \left(1 - \frac{i_{corr}}{i_{corr}^0}\right) \times 100 \quad (1)$$

where, i_{corr}^0 and i_{corr} represent the corrosion current densities in the absence and presence of $Zn_3(Ta_{1-x}Nb_x)_2O_8$ (where $x = 0; 0.05; 0.1; 0.5$ and 1) nanomaterials.

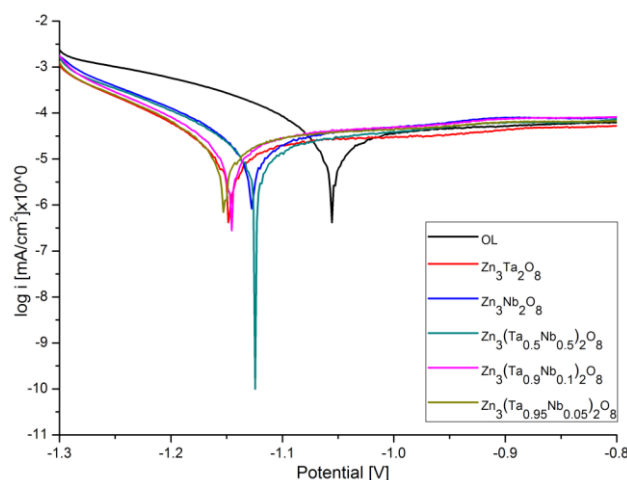


Fig. 10. Tafel representation of polarisation curves recorded in 0.1 mole/L Na_2SO_4 for the studied electrodes, $v = 1$ mV/s.

Table 3. Tafel parameters calculated for the investigated electrodes, after 30 minutes immersion in 0.1 mole/L Na_2SO_4 solution.

Electrode	E_{corr} [V]	i_{corr} [$\mu A/cm^2$]	R_p [$kohm \cdot cm^2$]	v_{cor} [$\mu m/Y$]	IE [%]
Bare OL	-1.05	40.36	0.90	469.1	-
$Zn_3Ta_2O_8$	-1.15	17.56	1.63	204.1	56.49
$Zn_3(Ta_{0.5}Nb_{0.5})_2O_8$	-1.12	18.91	1.44	219.8	53.15
$Zn_3(Ta_{0.9}Nb_{0.1})_2O_8$	-1.15	22.86	1.15	265.7	43.36
$Zn_3(Ta_{0.95}Nb_{0.05})_2O_8$	-1.15	23.37	1.26	271.6	42.09
$Zn_3Nb_2O_8$	-1.13	26.36	1.15	306.4	34.68

The current density corresponds to the rate of electrochemical reactions associated with corrosion processes taking place on OL surface, under polarization in 0.1 mole/L Na_2SO_4 media.

With respect to $Zn_3(Ta_{1-x}Nb_x)_2O_8$ compounds, in which both Ta and Nb are present, the anti-corrosion performance of the electrode was significantly improved, especially when the ratio between the Ta to Nb ions was 0.5 : 0.5 - the case of $Zn_3(Ta_{0.5}Nb_{0.5})_2O_8$.

The presence on the metal surface of Ta ions next to Zn ones (Ta:Zn ratio = 2:3), decreases the corrosion current density to $17.56 \mu A/cm^2$. Such a reduction in corrosion current density indicates a decrease in corrosion rate and exhibits an inhibition efficiency of 56.49%. Furthermore, the polarization resistance (R_p) increases slightly from $0.9 \text{ kohm}\cdot\text{cm}^2$ for bare OL electrode to $1.63 \text{ kohm}\cdot\text{cm}^2$ for the $Zn_3Ta_2O_8$ best electrode and all the tested nanomaterials offer corrosion protection for carbon steel material (IE in the range 34.6-56.4%).

4. Conclusions

Three novel oxides $Zn_3(Ta_{0.5}Nb_{0.5})_2O_8$, $Zn_3(Ta_{0.9}Nb_{0.1})_2O_8$ and $Zn_3(Ta_{0.95}Nb_{0.05})_2O_8$ were obtained by the solid-state method using Ta_2O_5 , Nb_2O_5 and ZnO as the starting materials. The nanomaterials based on $Zn_3(Ta_{1-x}Nb_x)_2O_8$ (where $x=0; 0.05; 0.1; 0.5$ and 1) have been characterized by means of various analytical techniques: XRD, FT-IR, SEM/EDAX, AFM, UV-VIS and PL.

From the XRD patterns the purity of the $Zn_3Ta_2O_8$ and $Zn_3Nb_2O_8$ nanomaterials can be certified. The specific peaks of the $Zn_3Nb_2O_8$ are present and displayed with increased signal by increasing the concentration of Nb in $Zn_3(Ta_{0.95}Nb_{0.05})_2O_8$, $Zn_3(Ta_{0.9}Nb_{0.1})_2O_8$ and $Zn_3(Ta_{0.5}Nb_{0.5})_2O_8$.

The FT-IR spectra show that by decreasing the amount of Nb from the nanomaterial composition, the corresponding Zn-O-Nb bond is shifted towards higher wavenumbers.

The SEM/EDAX measurements put into evidence various morphologies that are depending on the nature and chemical composition of the nanomaterials, such as: non-uniform and randomly dispersed spherical or ovoid and heavily compacted structures comprised of $Zn_3Ta_2O_8$ particles and uniform sized rods or blades of $Zn_3Nb_2O_8$ particles.

AFM measurements, especially the distribution of particle dimensions, indicate that the increase in Nb content causes a significant increase regarding the particle size. Besides, there is a direct relation between the higher content of Nb and the increased value of rugosity.

The values of the band gap that are decreasing in direct relationship with the increasing in Nb content were determined From UV-VIS spectra. PL spectra show that by increasing the Nb content, a more pronounced red shift is occurring, from 447 nm up to 460nm.

The electrochemical parameters spring from the Tafel curves show corrosion protection in the presence of all the $Zn_3(Ta_{1-x}Nb_x)_2O_8$ compounds, deposited on OL surface. The tests revealed that the corrosion protection is fairly good and that the electrode modified with $Zn_3Ta_2O_8$ presented a top inhibition efficiency of 56.49%.

Acknowledgements

This paper is supported by the Sectoral Operational Programme Human Resources Development (SOP HRD), financed from the European Social Fund and by the Romanian Government under the project number POSDRU/159/1.5/S/134378. The author Eugenia Fagadar-Cosma is acknowledging Romanian Academy for financial support in the frame of Programme 3 of ICT-AR.

References

- [1] Y.-C. Liou, H.-M. Chen, W.-C. Tsai, *Ceram. Int.* **35**, 2135 (2009).
- [2] X. Xiao, B. Yan, *Mater. Sci. Eng. B* **136**, 154 (2007).
- [3] Q.A. Shlyakhtin, Y.J. Oh, *J. Am. Ceram. Soc.* **89**, 3366 (2006).
- [4] M. Bîrdeanu, A.-V. Bîrdeanu, A.S. Gruia, E. Fagadar-Cosma, C.N. Avram, *J Alloy. Comp.*

- 573, 53 (2013).
- [5] A. Prasatkhetragarn, R. Yimnirun, S. Ananta, *Mater. Lett.* **61**, 3873 (2007).
- [6] YC. Liou, HM. Chen, WC. Tsai, *Ceram. Int.* **35**, 2135 (2009).
- [7] M.C. Wu, K.T. Huang, W.F. Su, *Mater. Chem. Phys.* **98**, 406 (2006).
- [8] S. K. Kurinec, P. D. Rack, M. D. Potter, *J. Mater. Res.* **15**, 1320 (2000).
- [9] P. D. Rack, M. D. Potter, S. Kurinec, W. Park, J. Penczek, B. K. Wagner, C. J. Summers, *J. Appl. Phys.*, **84**, 4466 (1998).
- [10] T. H. Noh, I.S. Cho, S. Lee, D. W. Kim, S. Park, S. W. Seo, C. W. Lee, K. S. Hong, *J. Am. Ceram. Soc.*, **95**(1), 227 (2012).
- [11] S.S. Pitale, L.L. Noto, I.M. Nagpure, O.M. Ntwaeaborwa, J.J. Terblans, H.C. Swart, *Adv. Mater. Res.*, **306-307**, 251 (2011).
- [12] C. A. Kondoleon, P. Rack, E. Lambers, P. Holloway, *J. Vac. Sci. Technol. A* **18**, 2699 (2000).
- [13] P. H. Holloway, T. A. Trottier, B. Abrams, C. Kondoleon, S. L. Jones, J.S. Sebastian, W. J. Thomes, *J. Vac. Sci. Technol. B*, **17**, 758 (1999).
- [14] P. H. Holloway, J. Sebastian, T. Trottier, H. Swart, *Solid State Technol.*, **38**, 47 (1995).
- [15] I. N. Shabanova, F. F. Chausov, E. A. Naimushina, I. S. Kazantseva, *J. Struct. Chem+*, **52**, S109 (2011).
- [16] T. V. Tsukanova, Thesis Dr. Tech. Sci., MEI, Moscow, 2007
- [17] M. Zemanová, *Chem. Pap.* **63**, 574 (2009).
- [18] S. Yogesha, A. Chitharanjan Hegde, *T. Indian I. Metals* **63**, 841 (2010).
- [19] Yu. S. Gerasimenko, M. V. Nechai, N. A. Belousova, *Mater. Sci.* **35**, 273 (1999).
- [20] A.P. Patil, R.H. Tupkary, *T. Indian I. Metals* **62**, 71 (2009).
- [21] A. Roshanghias, M. Heydarzadeh Sohi, *J. Coat. Technol. Res.*, **9**, 215 (2012).
- [22] H. Shi, F. Liu, E. Han, Y. Wei, *J. Mater. Sci. Technol.* **23**, 551 (2007).
- [23] A. P. I. Popoola, O. S. I. Fayomi, *International Journal of the Physical Sciences* **6**, 2447 (2011).
- [24] A.E. Elsherief, M.A. Shoebi, *J. Corrosion Prev. Control* (2003) 25.
- [25] R.A. Graham, R.C. Sutherland, *Proceedings of the international Symposium Niobium 2001, Niobium (2001) Ltd, Bridgeville, USA*, 337-355.
- [26] J.-P. Masse, H. Szymanowski 1, O. Zabeida, A. Amassian, J.E. Klemberg-Sapieha, L. Martinu, *Thin Solid Films* **515**, 1674 (2006).
- [27] K. Kamada, M. Mukai, Y. Matsumoto, *Electrochimica Acta* **49**, 321 (2004).
- [28] *International Centre for Diffraction Data PDF-4+*, 2008
- [29] www.ill.eu/sites/fullprof/.
- [30] T. Minami, H. Sato, K. Ohashi, T. Tomofuji, S. Takata, *J. Cryst. Growth* **117**, 370 (1992).
- [31] J.Z. Kong, A.D. Li, H.F. Zhai, Y.-P. Gong, H. Li, D. Wu, *J. Solid State Chem.* **182**, 2061 (2009).
- [32] V. Kapaklis, P. Pouloupoulos, V. Karoutsos, Th. Manouras, C. Politis, *Thin Solid Films*, **510**, 138 (2006).
- [33] P. Kubelka, F. Munk, Ein Beitrag zur Optik der Farban-striche, *Zh. Tekh. Fiz.* **12**, 593 (1931).
- [34] P. Kubelka, Part I, *J. Opt. Soc. Am.* **38**, 448 (1948).
- [35] P.D. Rack, M.D. Potter, S. Kurinec, W. Park, J. Penczek, B.K. Wagner, C.J. Summers, *J. Appl. Phys.* **84**, 4466 (1998).
- [36] Z. Ahmad, *Principles of Corrosion Engineering and Corrosion Control*, Butterworth-Heinemann/ICHEME Series. Elsevier, Amsterdam (2006) 377.